Available online at www.sciencedirect.com
SCIENCE DIRECT®
Journal of Nuclear Materials 353 (2006) 177–189
journal of nuclear materials
www.elsevier.com/locate/jnucmat

Characterization and modeling of creep mechanisms in Zircaloy-4

J.H. Moon [a], P.E. Cantonwine [b], K.R. Anderson [b], S. Karthikeyan [a], M.J. Mills [a,*]

[a] *Department of Materials Science and Engineering, The Ohio State University, 477 Watts Hall, 2041 College Road, Columbus, OH 43210, USA*
[b] *Bettis Atomic Power Laboratory, Bechtel Bettis, Inc., P.O. Box 79, West Mufflin, PA 15122, USA*

Received 14 September 2005; accepted 30 January 2006

Abstract

The deformation microstructure and creep mechanisms of Zircaloy-4 have been investigated. Four Zircaloy-4 specimens were tested at different temperatures and stress levels and the deformation microstructures of these specimens were analyzed using transmission electron microscopy. On the basis of microstructural observation of **a**-type screw dislocations in prismatic slip systems, the modified jogged-screw model has been applied as a rate controlling mechanism for creep of Zircaloy-4. In addition, the stress dependency of dislocation density, jog spacing, and jog height has been evaluated via modeling and experimental observations. The purpose of this study is to provide a detailed understanding of the creep deformation of Zircaloy-4 and prediction of creep rates in this alloy based on the microstructural information obtained from TEM analysis.

1. Introduction

Alpha-zirconium (HCP, α-Zr) alloys have over a 50-year history as a nuclear core material, but the underlying thermal creep mechanisms are still in question [1]. Although deformation during in-reactor operation is generally controlled by irradiation creep, thermal creep does dominate deformation at high temperatures or stresses representative of some design events (e.g., LOCA). In addition, during post-irradiation events such as repository storage, thermal creep dominates, although it is affected by irradiation damage [2]. Finally, understanding the mechanisms of thermal creep will provide a foundation for the eventual understanding of mechanisms for irradiation creep and post-irradiation creep.

Recently Hayes et al. [3] and Nam et al. [4] have attempted to examine the mechanism of thermal creep in α-Zr alloys. Hayes et al. [3] collected relevant creep data found in the literature for α-Zr tested for temperatures between 400 °C and 800 °C. Despite differences in impurity content and testing methods, they found that at high stresses the data overlapped when normalized using the familiar Bird–Mukherjee–Dorn equation. In addition, the slope of the data on the plot of normalized strain rate versus stress was

* Corresponding author. Tel.: +1 614 292 7514; fax: +1 614 292 1537.
E-mail address: mills.108@osu.edu (M.J. Mills).

0022-3115/$ - see front matter © 2006 Elsevier B.V. All rights reserved.
doi:10.1016/j.jnucmat.2006.01.023

6.4, which is in the range of five-power-law creep. The deformation mechanism associated with this regime is a recovery mechanism where dislocation substructure forms during primary creep via climb of edge dislocations. Steady state occurs when the substructure reaches an equilibrium configuration. The authors site literature evidence of substructure formation during creep of α-Zr further suggesting that creep deformation in the high stress regime is controlled by dislocation climb. At lower stresses, the stress exponent indicated that a diffusion mechanism such as Harper-Dorn or Coble creep controlled deformation.

Nam et al. [4] investigated the creep mechanism specifically for Zircaloy-4 in both the stress-relieved and recrystallized states for a test temperature range of 360–400 °C. Similar to Hayes et al., it was concluded that Zircaloy-4 deforms by a dislocation climb mechanism at high stress and a diffusional mechanism (likely Coble creep) at low stress. The microstructural evidence at low stress and strain (90 MPa, 0.8%, 400 °C) indicated no subgrain structure, supporting a diffusional mechanism. However, subgrain structure was observed at high stress and strain (150 MPa, 23%, 400 °C), supporting the dislocation climb mechanism.

In parallel, recent work on alpha-titanium (HCP, α-Ti) alloys has provided evidence that the non-conservative motion of jogged-screw dislocations controls steady-state creep deformation [5,6]. Because α-Ti and α-Zr have an HCP crystal structure with similar (c/a) ratios, for which prismatic slip is favored, it is logical to assume that the creep behavior and mechanisms may also be similar. In 1968, Ardell [7] suggested that the jogged-screw-related mechanism of Barrett and Nix [8] might control creep deformation in α-Zr. Their creep mechanism formulation included an assumed jog height on the order of a Burgers vector (b). However, the recent work on α-Ti [5,6] has shown that the heights of jogs are not on the order of a Burgers vector as assumed by Barrett and Nix [8], but rather the jog heights are actually on the order of a $100b$; that is, the jogs are likely much taller than previously assumed for α-Zr.

Clearly, there is still controversy over the exact mechanisms controlling creep deformation in α-Zr alloys (e.g., dislocation climb or glide). One shortcoming of the conclusion that creep is controlled by dislocation climb is that the observations of the substructure were made on test specimens with significant levels of strain. In the case of Hayes et al. [3] and Nam et al. [4], the observation of substructure was made on creep specimens with over 20% strain, even though steady-state creep is reached typically by 1% strain. In this study, we have focused on the early stages of creep in order to more readily characterize the dislocation structures present. We nevertheless consider the mechanisms identified below to be applicable to the steady-state regime.

Before describing the experimental aspects of the present study and the results, the modified jogged-screw model developed by Viswanathan et al. [9], and refined by Karthikeyan et al. [10] will be presented since we believe it to be highly relevant to creep of Zircaloy-4. The three deformation mechanisms related to the motion of jogged-screw dislocations will also be described: (1) jog dragging, (2) dipole dragging, and (3) dipole bypass. The remainder of the present paper will discuss the experimental results on creep tested Zircaloy-4, and the application of the presented modified jogged-screw model to this and other zirconium alloys as a function of temperature and stress. Following this will be a brief discussion on the implications of the observations to modeling irradiation creep behavior of alpha-zirconium alloys.

2. Background of proposed creep model

2.1. The modified jogged-screw model

The modified jogged-screw (MJS) model was initially developed based on observations of tall jogs in γ-TiAl [9]. The model is a modification of the jogged-screw model developed by Barrett and Nix [8]; essentially replacing an assumed jog height, b, with the actual jog height, h. The basic assumption of the model is that under steady-state conditions the chemical drag force (f) of the tall jog will be balanced by applied force on the dislocation line length between two tall jogs (τbl); where τ is the applied shear stress on the glide plane, b is the Burgers vector and l is the distance between two tall jogs. The glide velocity of screw dislocations with tall jogs of height, h is given as [9]:

$$v_s = \left(\frac{4\pi D_s}{h}\right)\left[\sinh\left(\frac{\tau\Omega l}{hkT}\right)\right], \tag{2.1}$$

where D_s is the self-diffusion coefficient, Ω is the atomic volume, k is the Boltzman's constant, and T is the temperature in Kelvin.

A shortcoming of this model is that the tall jog is assumed to be a point source/sink of vacancies rather than a more physically meaningful finite line

source/sink. Karthikeyan et al. [10] corrected this shortcoming resulting in a revision of Eq. (2.1):

$$v_s = \left(\frac{4\sqrt{2}\pi D_s}{b\delta(h)}\right)\left[\sinh\left(\frac{\tau\Omega l}{hkT}\right)\right], \tag{2.2}$$

where $\delta(h)$ is a logarithmic function of h and b:

$$\delta(h) = 0.17 + 4.528\ln\left(\frac{h}{b}\right). \tag{2.3}$$

The steady-state creep rate is then related to the dislocation velocity via the Orowan equation:

$$\dot{\gamma} = \rho b v_s, \tag{2.4}$$

where ρ is the density of mobile dislocations, which appears to follow the Taylor equation for the systems studied thus far [10]:

$$\rho = \left(\frac{\tau}{\alpha G b}\right)^2, \tag{2.5}$$

where G is the shear modulus and α is the Taylor factor. Converting the shear strain rate and shear stress to tensile strain rate and stress ($\dot{\varepsilon} = \dot{\gamma}/2$ and $\sigma = 2\tau$) and substituting Eqs. (2.2) and (2.5) into the Orowan equation gives:

$$\dot{\varepsilon} = \left(\frac{2\sqrt{2}\pi b D_s}{\delta(h)}\right)\left(\frac{\sigma}{2\alpha G b}\right)^2\left[\sinh\left(\frac{\sigma\Omega l}{2hkT}\right)\right]. \tag{2.6}$$

2.2. Jog dragging, dipole dragging, and dipole bypass

Viswanathan et al. [9] and Karthikeyan et al. [10] suggested that there are three possible scenarios for the motion of jogged-screw dislocations as a function of jog height (Fig. 1). When the jog is relatively short, jog dragging is relatively easy. As the jog becomes taller, the stress required for jog dragging increases significantly making the extension of a dipole (dipole dragging) more favorable. When the jog grows even taller, the applied stress is sufficient to break the dipole, which may then act as a dislocation source (as the near-edge segments attached to the jog bypass each other).

Under creep conditions, the stress required for each of these rate-controlling processes can be evaluated as a function of jog height. Fig. 2 shows the jog height as a function of jog velocity for these three processes for Zircaloy-4. Note that the jog dragging process is strongly temperature dependent, while the other two processes only depend weakly on temperature (through the elastic modulus). The

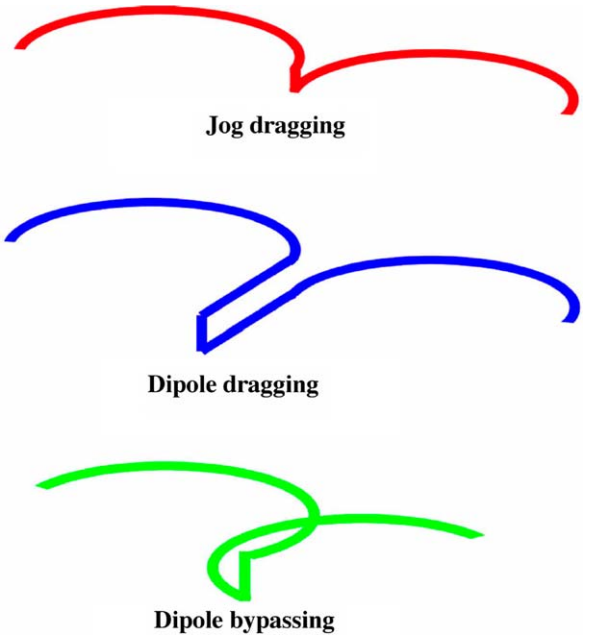

Fig. 1. The three possible mechanisms as a function of jog height; jog dragging at short jog heights, dipole dragging at intermediate jog heights, and dipole bypassing at large jog heights [5].

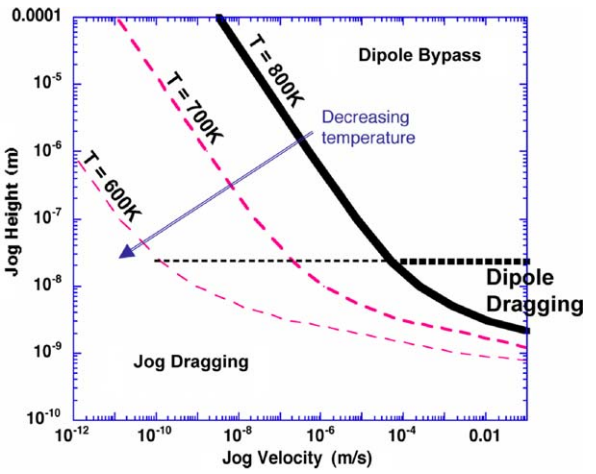

Fig. 2. Map indicating the most energetically favorable mechanism for a combination of jog height, jog velocity, and temperature (for Zircaloy-4).

salient features of this plot is that at higher temperatures and low stresses, the first deformation process which occurs as the jogs begin growing in height is jog dragging, eventually transitioning to dipole bypass. However, at larger dislocation velocities caused by higher stress or at lower temperatures, dipole dragging can intervene and dominate

between the jog dragging and dipole bypass processes.

3. Experimental procedure

3.1. Materials

The alloy chosen for this study was rolled Zircaloy-4 slow quenched from the β phase field using a proprietary process. The resulting microstructure was the Widmanstätten structure typical of β-quenched Zircaloy. The texture was not measured, but is expected to be close to random [11]. Creep testing was performed parallel to the rolling direction.

3.2. Creep testing

Four round Zircaloy-4 creep specimens (6.4 mm diameter, 76 mm gauge length) were dead-load tested at the following temperatures/initial applied stress levels: 260 °C/165 MPa, 371 °C/122 MPa, 510 °C/83 MPa and 593 °C/42 MPa. Table 1 shows the applied stresses and other creep test parameters and results. Tests at 260 °C and 371 °C were performed in air, while tests at 510 °C and 593 °C were performed in a flowing Argon atmosphere. No significant oxidation of specimens was observed after testing. The stress on the sample tested at 260 °C was increased to 168 MPa after 316 h. All tests were terminated by cooling under load.

3.3. Transmission electron microscopy

The crept specimens were sectioned such that the foil plane was approximately 45° to the loading axis. The purpose of this sectioning is that occasionally the principal glide plane will coincide with the foil plane, so that the dislocation morphology can be more readily characterized. Additional details regarding dislocation density and jog spacing measurements are provided in Section 5.1. The foils were prepared by twinjet thinning technique using an electro-polishing solution consisting of 470 ml methanol, 30 ml sulfuric acid, and 1.2 ml hydrofluoric acid, at a voltage of either 21–22 V and a temperature of −35 to −30 °C or ~25 V and a temperature of −26 °C. Some hydride particles resulted from this electro-polishing process, but they were easily distinguishable from dislocations. Observations of the deformation structure were conducted on a Philips CM200 transmission electron microscope with LaB_6 cathode operated at an accelerating voltage of 200 kV.

4. Experimental results of creep tested Zircaloy-4

4.1. Creep data

Fig. 3 shows the creep curves of four Zircaloy-4 test specimens. The measured steady-state creep rates are given in Table 1. Specimens crept at 510 °C and 593 °C had similar steady-state creep rates of $\sim 10^{-8}$ s^{-1}. Specimens crept at 260 °C and 371 °C had steady-state creep rates about an order of magnitude lower. However, the relative amount

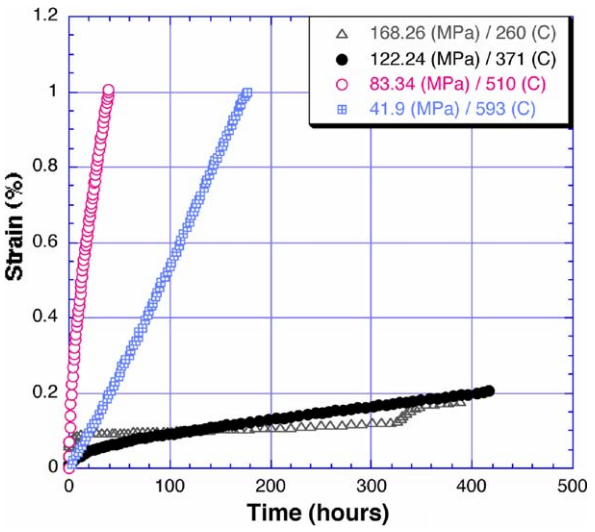

Fig. 3. Creep strain vs. time for Zircaloy-4 specimens crept at four different conditions.

Table 1
Creep test results of Zircaloy-4 specimens

Specimen number	Temp., °C	Time of test, h	Total creep, %	Load, lbs	Stress, MPa	Steady-state strain rate, s^{-1}
5037	260	398.2	0.18	1190/1210	165/168	2×10^{-10}
5038	371	412.9	0.202	880	122	1×10^{-9}
5039	510	39.4	1.0	600	83	5×10^{-8}
5041	593	178.2	1.0	300	42	1.5×10^{-8}

of transient strain decreased as the test temperature increased; at 260 °C, the transient creep strain was large, consistent with creep data reported by Ecob and Donaldson [12], and at 593 °C, there is almost no transient creep. In addition, the specimen creep tested at 260 °C and 165 MPa was uploaded to 168 MPa after 316 h and showed normal transient creep after the stress-jump.

4.2. Creep microstructures (TEM observations)

4.2.1. Low temperature regime – jog dragging/ dipole dragging

It is well known that the principal slip systems in zirconium and its alloys are of the type $\frac{a}{3}\langle 2\bar{1}\bar{1}0\rangle\{0 1\bar{1}0\}$. In addition, **a**-type dislocations can be mixed edge and screw in character, but the screw orientation tends to dominate. Figs. 4 and 5 show examples of the substructure of Zircaloy-4 crept at 260 °C and 165 MPa. Two different families of **a**-type dislocations oriented close to their screw directions (determined via line trace analysis) are observed, containing numerous cusp features that appear to be associated with jogs (e.g., in Fig. 5(b)). A sense of the dislocation character can be ascertained from the direction of the operating diffraction **g**-vector (indicated in the TEM images) relative to the dislocation line direction: the dislocation segments more parallel to the **g**-vector are screw in character, and those more orthogonal are edge in character. There are also relatively straight, elongated features along the third $\langle 1 1\bar{2}0\rangle$ direction (Fig. 5(c)). These appear to be extended dipoles dragged out from jogs on the **a**-type screw dislocations. The straight dipoles are typified by a strong difference in contrast/width for the $\pm\mathbf{g}$ conditions of Fig. 5(a) and (b). This observation is consistent with a dipole dragging mechanism discussed in Section 2. At lower temperature, the dipole dragging mechanism in Fig. 2 dominates almost the entire jog velocity range for taller jog heights. However, notice that smaller jogs are still expected to be limited by jog dragging, based on Fig. 2. Therefore, the evidence of apparent dipole dragging supports the formation and existence of jogged-screw configurations during creep of this alloy. However, at this low temperature and high stress, dipoles are formed after the jogs reach a moderate height, and before dipole bypass occurs. There also appears to be small debris loops and/or zirconium hydride precipitates similarly aligned. Fig. 5 shows the same dislocations under different diffracting conditions.

4.2.2. Intermediate temperature regime – jog dragging

Figs. 6 and 7 show bright-field micrographs of the microstructure of Zircaloy-4 that was crept at 371 °C and 122 MPa. Based on Fig. 2, the region for which the dipole dragging mechanism dominates is expected to shrink as temperature increases. At the test temperature of 371 °C, a transition directly from jog dragging to dipole bypass is more likely than a transition through the dipole dragging mechanism region. This is supported by dislocation configurations that show that extended dipole features are easily pinched off and divided into a number of small loops.

Dislocations in a screw orientation, formation of loops, and bowed segments are frequently observed in Fig. 6. The initial formation of an apparent dislocation network can also be seen in Fig 6(c). Fig. 6(a) shows significantly bowed segments in one

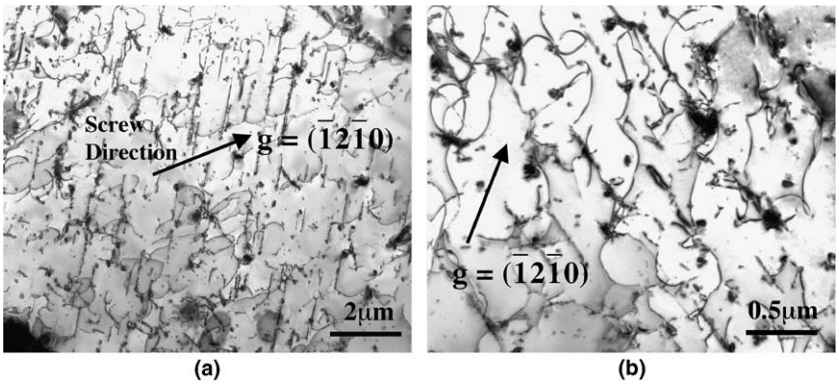

Fig. 4. Bright-field TEM micrographs of Zircaloy-4 crept at 260 °C and 165 MPa taken (a) with a $[10\bar{1}1]$ beam direction and (b) at higher magnification with a $[10\bar{1}0]$ beam direction.

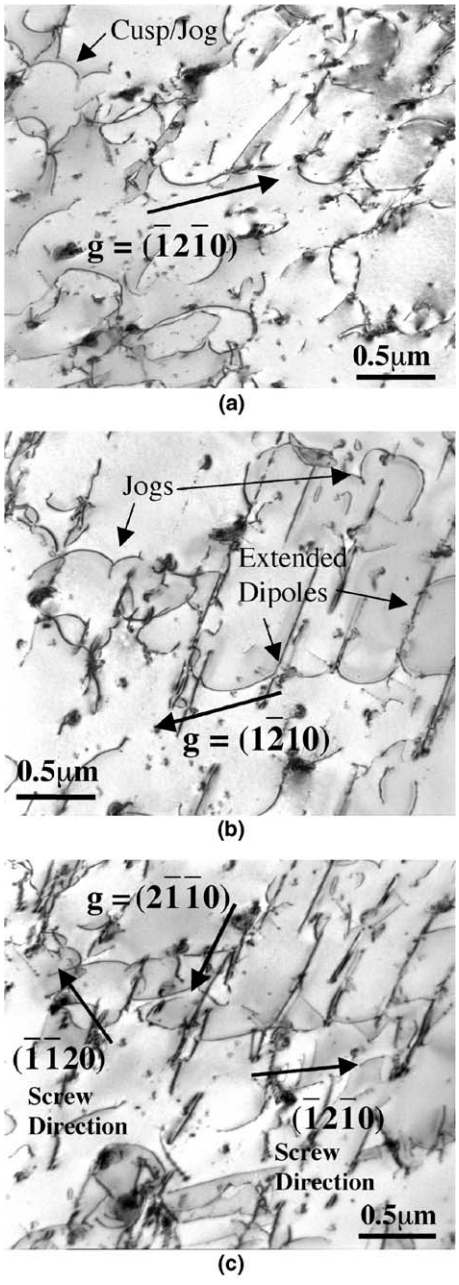

Fig. 5. Bright-field TEM micrographs of Zircaloy-4 crept at 260 °C and 165 MPa taken (a) with a $[10\bar{1}0]$ beam direction, (b) with a $[10\bar{1}1]$ beam direction, and (c) with a [0001] beam direction.

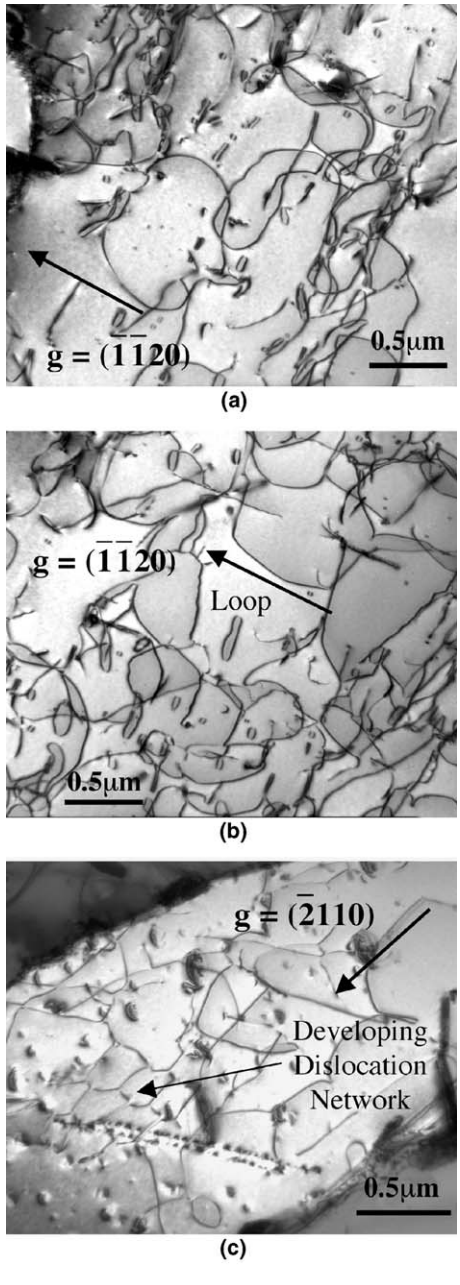

Fig. 6. Bright-field TEM micrographs of Zircaloy-4 crept at 371 °C and 122 MPa taken with a $[1\bar{1}00]$ beam direction (a, b), and with a [0001] beam direction (c). An incipient dislocation network can be seen in (c).

dislocation line, and Fig. 6(b) shows a number of dislocation loops, which appear to be debris generated by the pinching off of partially extended dipoles during deformation (i.e. they were not present prior to testing). This conclusion is supported by a pair of images acquired at $+\mathbf{g}/-\mathbf{g}$ diffracting (tilt) conditions, as shown in Fig. 7(a) and (b). Note the change in apparent width of the debris loops, demonstrating that they are narrow, complete loops. Loops A, B, and D are the same 'sign', while loop C is of opposite 'sign'. Fig. 7(c) also shows evidence of a tall jog, which is approximately 100 nm in height.

Figs. 8–11 show examples of the microstructure of the Zircaloy-4 specimen crept at 510 °C and 83 MPa.

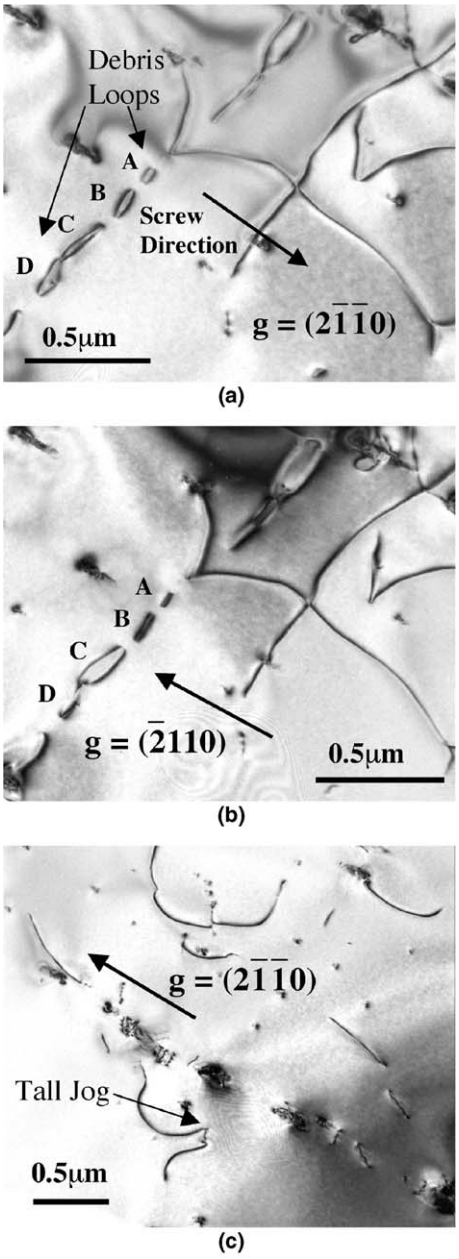

Fig. 7. Bright-field TEM micrographs of Zircaloy-4 crept at 371 °C and 122 MPa taken with a [0$\bar{1}$10] beam direction, (a, b), showing debris loops, and with a [0$\bar{1}$11] beam direction (c), showing evidence of a tall jog (~100 nm in height).

Fig. 8 shows low magnification TEM images of the test specimen, in which the foils were cut from the grip and gauge section, respectively. Almost identical sub-grain structures are observed in both images. This shows that a number of low-angle boundaries already existed before the specimens were crept. The TEM images of Fig. 9 clearly reveal frequent cusps in the **a**-type screw dislocations and bowed segments between pinning points.

The overall dislocation configuration observed in the TEM images of the Zircaloy-4 specimen creep tested at 510 °C and 83 MPa is similar to that observed for the specimen tested at 371 °C and 122 MPa; however, evidence of extended dipole features is less obvious. Thus, the dipole dragging process appears to become less probable at higher temperature and lower jog velocity. Fig. 10 shows a slightly higher dislocation density and relatively straight dislocations compared to Fig. 9. Fig. 10(b) also shows dislocation interactions and a tendency toward dislocation network formation in this specimen, which was examined at a strain level of about 1%.

Fig. 11 shows images of the same area with different diffracting conditions, proving the presence of at least two families of dislocations. In Fig. 11(b), the more steeply inclined family of dislocations (determined from TEM tilting experiments) is out of contrast, consistent with these having a Burgers vector that is different from the dislocation family lying largely in the foil plane.

4.2.3. High temperature regime – substructure formation

Figs. 12 and 13 show bright-field TEM micrographs of the microstructure of the Zircaloy-4 specimen crept at 593 °C and 42 MPa. Fig. 12(a) shows relatively straight boundary edge dislocations. In Fig. 12(b), dislocations are elongated in the screw orientation and appear to be pinned along their length and have an apparent lower dislocation density compared to the previous specimens. Also, larger, oval shaped hydride precipitates and a number of smaller hydride precipitates due to specimen preparation can be observed.

The TEM images of Fig. 13 show relatively straight lines without significant bowed segments and some evidence of dislocation network formation. This is evidence of general climb occurring at this temperature. Only the image of Fig. 12(b) shows some evidence of jog dragging taking place.

5. Discussion

5.1. Application of model to (non-irradiated) Zircaloy-4

On the basis of the above TEM observations, the deformation microstructure of crept Zircaloy-4

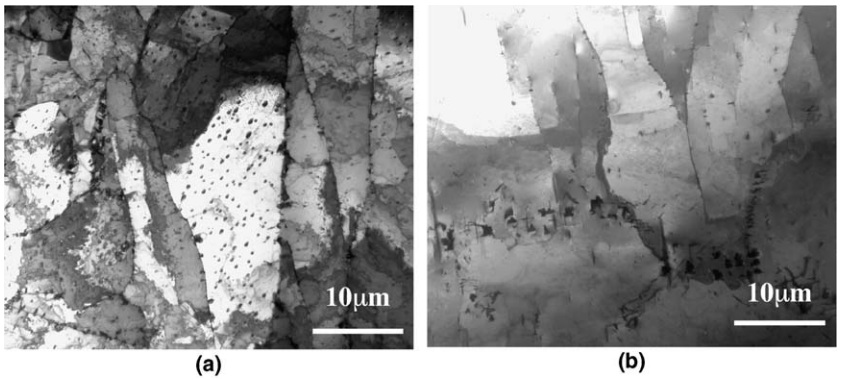

Fig. 8. Bright-field TEM micrographs of Zircaloy-4 crept at 510 °C and 83 MPa showing microstructures from (a) the grip section and (b) the gauge section.

shows that for a range of temperatures the dislocation substructure of this alloy is quite similar to that which has been observed in several crept titanium alloys (γ-TiAl [9], Ti-6242 [6] and Ti-6Al [5]). The modified jogged-screw model has been proposed as the rate-controlling mechanism for these titanium alloys. Thus, it is clear that the applicability of this model to Zircaloy-4 is very promising.

After considering the HCP crystal structure for case of Zircaloy-4, Eq. (2.6) can be modified to give the following expression:

$$\dot{\varepsilon} = b \cdot \left(\frac{2.9\pi}{\delta(h)}\right) D_0 \times \exp\left(-\frac{Q_{SD}}{kT}\right)\left(\frac{\sigma}{2\alpha G b}\right)^2 \left[\sinh\left(\frac{\sigma \Omega l}{2hkT}\right)\right], \quad (5.1)$$

where D_0 is pre-exponential constant, and Q_{SD} is activation energy for self-diffusion. This equation can predict the steady-state strain rate at a given applied stress if all the microstructural parameters such as jog height, jog spacing, and dislocation density are known.

At steady state, these microstructural parameters appear to be dependent only on applied stress [10]. The dislocation density is expressed by the Taylor equation in Eq. (2.5). This was confirmed with measurements of dislocation density, which are plotted in Fig. 14(a) as a function of resolved shear stress. The dislocation densities were measured by determining the total line lengths in about five separate fields of view of similarly oriented grains. Foil thickness was determined from convergent beam electron diffraction pattern analysis. The grains analyzed were those with the primary glide plane parallel to the foil plane. Since the samples were prepared from sections prepared at 45° from the tensile axis, the Schmid factors for these slip systems were invariably close to 0.5, and the actual applied shear stress acting in each grain sampled could be determined. The value of the Taylor factor (α) of 1.0 provides a good fit to the observed dislocation densities. Table 2 shows the measured average values of dislocation density, and examples of some of the images used for these measurements. Because of the relative distribution of dislocations and the general absence of substructure that could limit dislocation motion, it seems reasonable that the measured dislocation density represents the mobile dislocation density.

Karthikeyan et al. [10] also suggested that jog spacing is inversely proportional to the applied stress. Table 3 gives the values of average jog spacing for all the specimens as measured, generally from the same TEM micrographs that were used to determine dislocation densities. Care was taken to make these measurements while viewing the foils perpendicular to the dislocation glide plane. Fig. 14(b) shows a plot of the average jog spacing data. As gleaned from Fig. 14(b), the average jog spacing is also inversely proportional to the applied stress for Zircaloy-4, and obeys the following general expression:

$$l = A\tau^{-1}, \quad (5.2)$$

where A is a proportionality constant.

Karthikeyan et al. [10] suggested that a reasonable estimation of the jog height was the critical height for the transition from jog dragging to dipole dragging. The critical stresses associated with jog dragging, dipole dragging, and dipole bypass are described by the following equations:

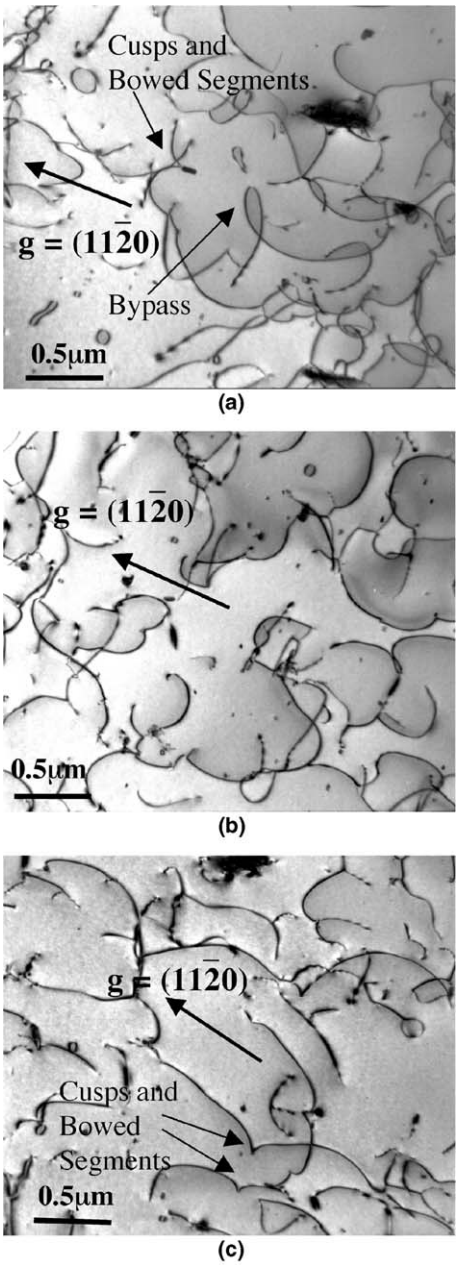

Fig. 9. Bright-field TEM micrographs of Zircaloy-4 crept at 510 °C and 83 MPa taken with a $[1\bar{1}00]$ beam direction, showing frequent cusps in dislocation lines along with bowed line segments and some evidence of dipole bypass.

$$\tau_{\text{bypass}} = Gb\left(\frac{1}{8\pi(1-v)h}\right), \tag{5.3}$$

$$\tau_{\text{dipole}} = Gb\left(\frac{1}{2\pi(1-v)l}\right)\ln\left(\frac{h}{b}\right) + \frac{E_{\text{core}}}{lb^2}, \tag{5.4}$$

$$\tau_{\text{jog}} = \frac{hkT\left[\arcsin h\left(\frac{vb\delta(h)}{4\pi Df}\right)\right]}{\Omega l}. \tag{5.5}$$

Using Eqs. (5.3)–(5.5), the minimum stress required to initiate each of these processes can be calculated as a function of the jog height. Fig. 15 is a map showing the minimum stress required as a function of jog height for each of three processes controlling dislocation motion at different jog velocities. Karthikeyan et al. [10] further showed that the appropriate jog height for the jog dragging model is related to stress via a power law model in the form of

$$h_{\text{d}} = L\tau^{a}, \tag{5.6}$$

where a appears to be -2.0 and L is a proportionality constant.

Incorporating the relationships for jog height, jog spacing, and dislocation density into Eq. (5.1) gives:

$$\dot{\varepsilon} = b\cdot\left(\frac{2.9\pi}{\delta(h)}\right)D_0 \times \exp\left(-\frac{Q_{\text{SD}}}{kT}\right)\left(\frac{\sigma}{2\alpha Gb}\right)^2\left[\sinh\left(\frac{\sigma^2\Omega A}{4LkT}\right)\right]. \tag{5.7}$$

Fig. 16 shows that the creep rate predictions are in good agreement with the experimental Zircaloy-4 creep data for the four different stresses and temperatures. Note that the model curves suggest that the two higher stress tests may have been conducted in the 'power-law breakdown' regime, although this higher stress exponent regime is a natural result of the model and is not the consequence of a mechanism change.

Fig. 17 shows a plot of strain-rate (compensated by D, k, G, b, and T) versus stress (compensated by G) containing model-calculated data and the present experimental data for Zircaloy-4. In addition, a best-fit line of extensive data from various creep studies on α-Zr and its alloys, as compiled by Hayes et al. [3], is overlaid on the plot of Fig. 17 for comparison purposes. Values for the shear modulus, G, of Zircaloy-4 were calculated from Eq. (5.8) [4]:

$$G = 42\,518.52 - 22.185T\ (\text{K}) \quad \text{MPa}. \tag{5.8}$$

Values for the diffusion coefficient, D were calculated from Eq. (5.9) [3]:

$$D = D_0\exp\left(\frac{-Q_{\text{SD}}}{RT}\right) \quad \text{m}^2/\text{s}, \tag{5.9}$$

where $D_0 = 5\times10^{-4}\ \text{m}^2/\text{s}$, and $Q_{\text{SD}} = 270\ \text{kJ/mol}$.

It is clear from Fig. 17 that the creep-rate data from the present study are much lower than the compiled literature data for α-zirconium [3], which

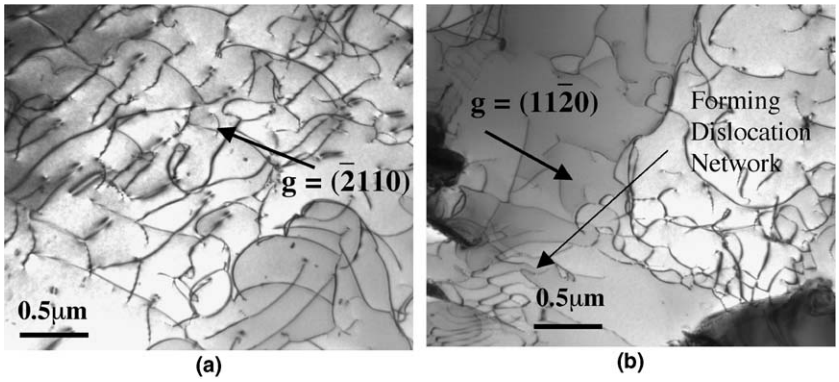

Fig. 10. Bright-field TEM micrographs of Zircaloy-4 crept at 510 °C and 83 MPa taken with a $[0\bar{1}10]$ beam direction, showing slightly higher apparent dislocation density compared to images of Fig. 9.

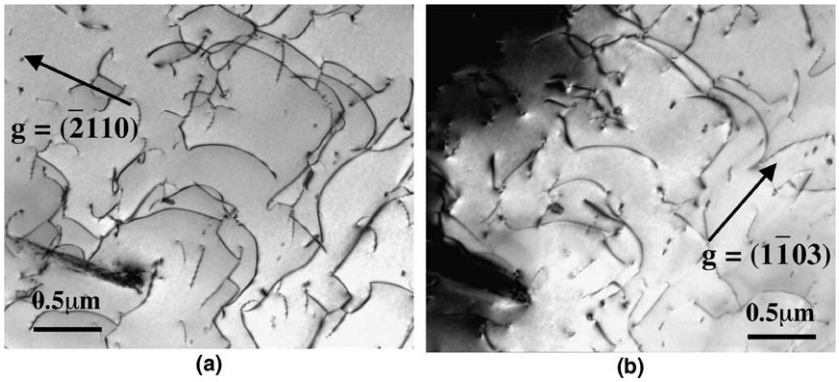

Fig. 11. Bright-field TEM micrographs of Zircaloy-4 crept at 510 °C and 83 MPa taken with (a) a $[0\bar{1}10]$ beam direction and (b) a $[1\bar{2}1\bar{1}]$ beam direction, showing two diffracting conditions proving the presence of at least two families of dislocations.

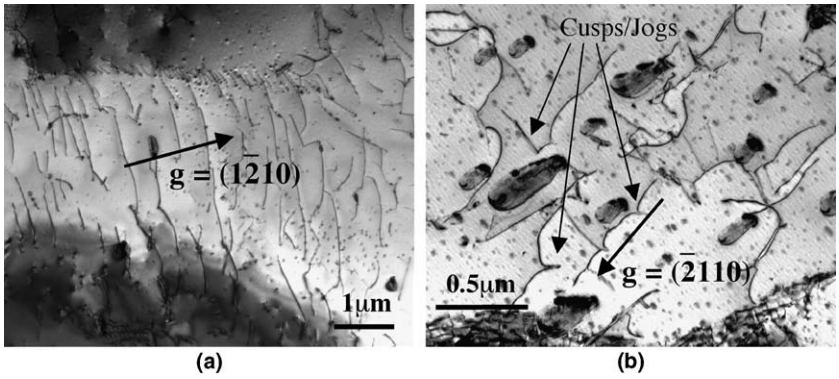

Fig. 12. Bright-field TEM micrographs of Zircaloy-4 crept at 593 °C and 42 MPa taken with (a) a $[30\bar{3}1]$ beam direction and (b) a $[0\bar{3}3\bar{1}]$ beam direction.

may be due to differences in thermo-mechanical processing and texture [13] and solute effects. However, the form of these normalized curves appear to be quite promising. The predicted stress exponent value is somewhat smaller than the value of 6 observed in the low σ/G regime. However, the

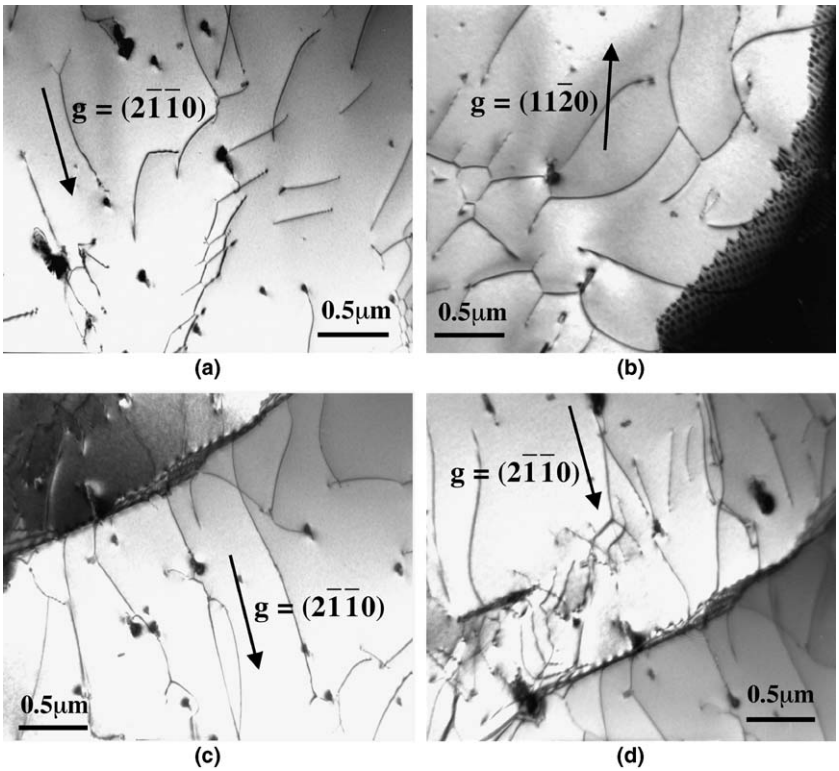

Fig. 13. Bright-field TEM micrographs of Zircaloy-4 crept at 593 °C and 42 MPa taken with (a) a [0$\bar{1}$10] beam direction, (b) a [1$\bar{1}$00] beam direction, (c) a [0$\bar{1}$10] beam direction, and (d) a [0$\bar{1}$10] beam direction.

higher stress exponent regime is predicted to occur at approximately the same value of σ/G. Additional creep testing over a wider range of stresses will be required to fully evaluate the model against the presently studied Zircaloy-4 alloy.

5.2. Implication of these observations to creep of irradiated Zircaloy-4

Following the terminology defined by Franklin et al. [14], three different phenomena make up irradiation creep; these are irradiation-retarded, irradiation-enhanced, and irradiation-induced creep. Irradiation-retarded creep represents the retarding effect of irradiation damage on thermal creep. Irradiation-enhanced creep is the flux enhancement of thermal creep in irradiated materials. Irradiation-induced creep is a separate mechanism that occurs in parallel with these thermal-creep based mechanisms. This separate mechanism involves a stress enhancement of the stress-free growth mechanism, which is related to the preferential formation of interstitial and vacancy loops on different planes relative to the applied stress [14,15]. Although the possibility of flux enhancement of the jog dragging mechanism has been recognized, in general, the mechanism identified with irradiation-enhanced creep has been climb-glide of edge dislocations [14,15]. In particular, Nichols discounted the jog dragging mechanism as he thought it did not explain the creep strengthening observed during irradiation-retarded creep since the screw dislocations could easily cross slip around the irradiation damage. His other criticism of the jog dragging mechanism was related to an analysis by Holmes [16] that the jogged-screw dislocation velocity reaches a limiting value with increasing stress rather than increasing exponentially (or by a hyperbolic sine); however, Holmes did not consider the effect of jog height.

The results presented herein support the tell-jog dragging mechanism, and thus warrant a rethinking of the mechanism of irradiation-retarded and irradiation-enhanced creep. To address Nichols' first criticism of the jog dragging mechanism, a scenario describing the interaction of jogged-screw dislocation with irradiation damage where irradiation-retarded

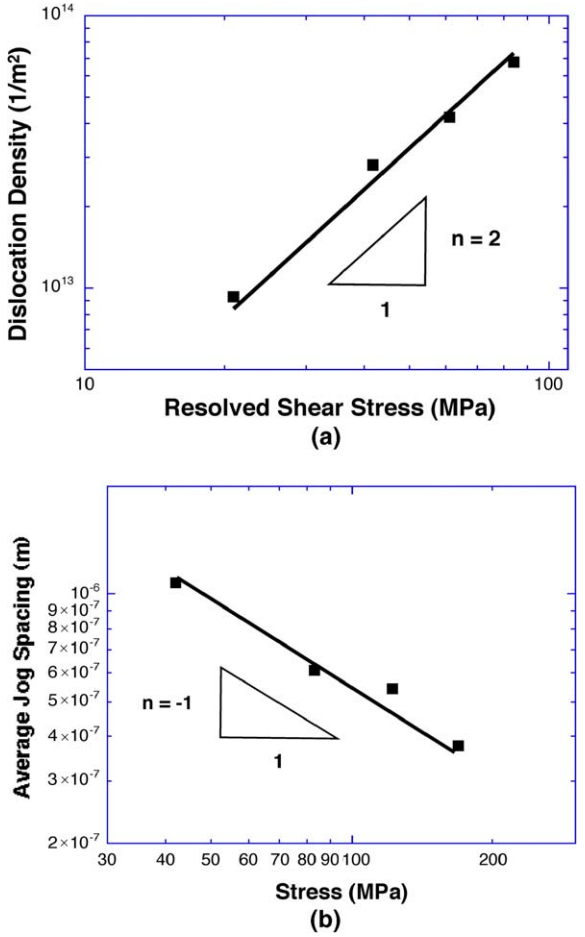

Fig. 14. Plot of (a) variation of dislocation density as a function of the resolved shear stress and (b) average jog spacing as a function of stress.

Table 2
Dislocation density measurements from TEM micrographs

Specimen number	Resolved shear stress, MPa	Dislocation density, m^{-2}	Image/figure number
5037	84	$6.7\times10^{+13}$	4
5038	61	$4.2\times10^{+13}$	6(b)
5039	42	$2.8\times10^{+13}$	10(a)
5041	21	$9.3\times10^{+12}$	12

Table 3
Results of jog spacing measurements from TEM micrographs

Specimen number	Resolved shear stress, MPa	Average jog spacing, nm	Image/figure number
5037	84	380	4
5038	61	540	6(c)
5039	42	610	Not shown
5041	21	1080	12(b)

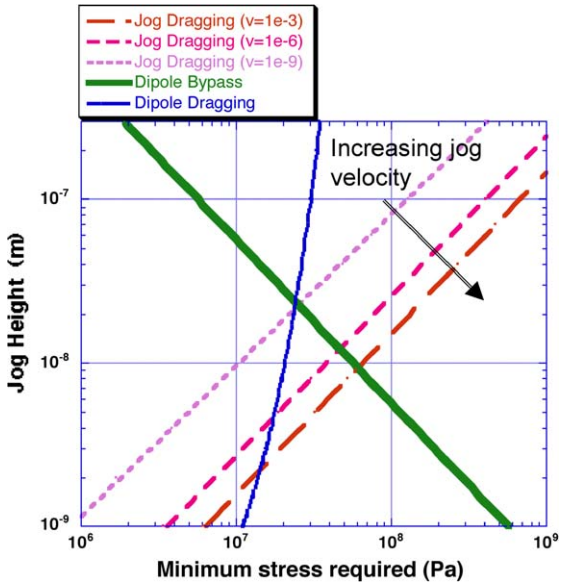

Fig. 15. The minimum stress required for each of the three processes for dislocation motion for different jog velocities together with jog heights.

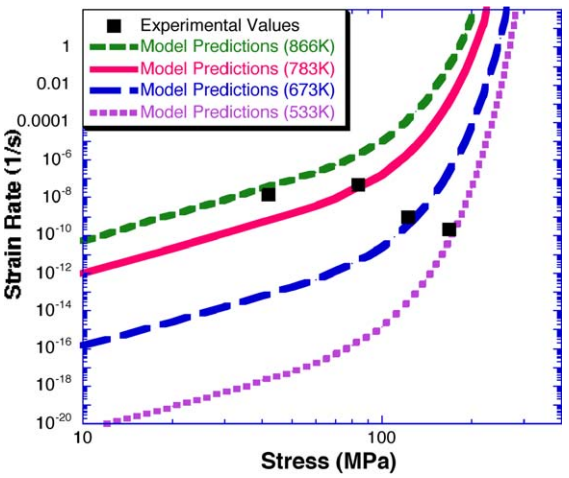

Fig. 16. Model predictions at 260 °C (533 K), 371 °C (644 K), 510 °C (783 K), and 593 °C (866 K). The creep rate predictions are in good agreement to experimental data.

creep dominates is as follows. Assuming the presence of tall jogs, the screw dislocations will bow causing the edge component of the dislocation to increase. When these bowed dislocations interact with irradiation damage, the screw component can cross-slip over the damage while the edge component must climb over the damage. Thus, the motion of the jogged-screw dislocation could be limited by the

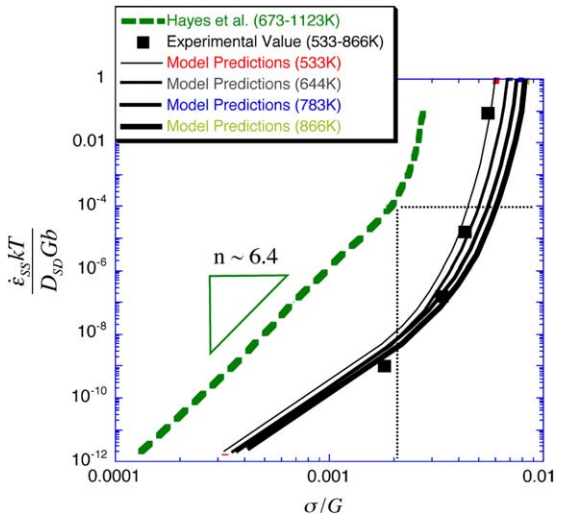

Fig. 17. Plot of normalized strain rate vs. normalized stress for model predictions at various temperatures together with creep data from the present study and previous studies of α-zirconium creep [3]. The transition to the power-law breakdown regime exhibited in the previous experiments is indicated.

climb of the edge components over the irradiation damage or by the jog dragging mechanism, dipole dragging mechanism, and/or dipole bypass mechanism. In addition, the effective increase in the resistance to glide would likely cause the average jog height to increase (since the jog height for dipole bypass would increase) – leading to an increase in the jog dragging force and decreasing creep rates compared to the non-irradiated case.

For the case of irradiation-enhanced creep, the effect of flux/fluence dependence on the velocity of the jogged-screw dislocation could be accounted for by including a flux/fluence dependence on the concentration of vacancies and interstitials (effectively increasing the diffusivity) in the model derivation. The increase in point defect concentration with flux/fluence would enhance the jog dragging mechanism at lower temperatures potentially suppressing the dipole dragging mechanism observed in non-irradiated Zircaloy at 260 °C.

6. Conclusions

1. Screw dislocations with tall jogs (~100*b*) are the predominant dislocations observed in Zircaloy-4 creep tested at 260 °C/165 MPa, 371 °C/122 MPa, 510 °C/83 MPa, which yielded steady-state strain rates in the range of 10^{-9}–10^{-8} s^{-1}.
2. Evidence of edge dislocations and dislocation networks increased as the test temperature, increased indicating a transition to a more general climb mechanism between 510 °C and 593 °C.
3. The modified jogged-screw model shows promise in predicting creep in Zircaloy.
4. Since irradiation-enhanced and irradiation-retarded creep typically occur at temperatures less than 510 °C, screw dislocations with tall jogs should be considered when trying to understand and model the effect of irradiation on creep in Zircaloy.

References

[1] K.L. Murty, JOM 52 (2000) 34.
[2] F.A. Nichols, J. Nucl. Mater. 30 (1969) 249.
[3] T.A. Hayes, M.E. Kassner, R.S. Rosen, Metall. Mater. Trans. A 33A (2002) 337.
[4] C. Nam, B.K. Choi, M.H. Lee, Y.H. Jeong, J. Nucl. Mater. 305 (2002) 70.
[5] G.B. Viswanathan, S. Karthikeyan, R.W. Hayes, M.J. Mills, Metall. Mater. Trans. A 33 (2002) 329.
[6] G.B. Viswanathan, S. Karthikeyan, R.W. Hayes, M.J. Mills, Acta Mater. 50 (2002) 4965.
[7] A.J. Ardell, J. Appl. Phys. 37 (1966) 2910.
[8] C.R. Barrett, W.D. Nix, Acta Metall. 13 (1965) 1247.
[9] G.B. Viswanathan, V.K. Vasudevan, M.J. Mills, Acta Mater. 47 (1999) 1399.
[10] S. Karthikeyan, G.B. Viswanathan, M.J. Mills, Acta Mater. 52 (2004) 2577.
[11] J.J. Kearn, Bettis Atomic Laboratory Report, WAPD-TM-472, 1965.
[12] R.C. Ecob, A.T. Donaldson, J. Nucl. Mater. 132 (1985) 110.
[13] K.L. Murty, B.L. Adams, Mater. Sci. Eng. 70 (1985) 169.
[14] D.G. Franklin, G.E. Lucas, A.L. Bement, ASTM STP 815, 1983, p. 72.
[15] F.A. Nichols, ASTM STP 939, 1987, p. 5.
[16] J.J. Holmes, Acta Metall. 15 (1967) 570.